Icarus

LunarSAR2O: SAR-to-Optical Image Translation for Permanently Shadowed Region Exploration and its Application

--Manuscript Draft--

Manuscript Number:	
Article Type:	Research paper
Keywords:	PSR; SAR; LunarS2OUNet; Moon; Optical Images
Corresponding Author:	Niutao Liu Key Laboratory for Information Science of Electromagnetic Waves, Ministry of Education, Fudan University CHINA
First Author:	Tong Xia
Order of Authors:	Tong Xia
	Niutao Liu
	Yi Zheng
	Ya-Qiu Jin
Abstract:	Permanently Shadowed Regions (PSR) at the lunar poles receive no direct sunlight due to the Moon's 1.54° axial tilt, making their study constrained by severe scarcity of optical imagery. Existing ShadowCam optical observations, affected by high-incidence-angle scattered light and topographic blocking, cannot adequately resolve morphological features within Secondary Shadowed Regions (SSR) or rock distributions. While Synthetic Aperture Radar (SAR) can image PSRs independently of illumination conditions and exhibits sensitivity to meter-scale rocks, challenges remain in interpreting its inherent speckle noise patterns and geometric distortions. The study produced the Lunar Optical-SAR Aligned Dataset (LOSAD-14k) containing 14,000 precisely aligned SAR-optical image pairs. The optical images in LOSAD-14k maintain identical incidence geometry with their SAR counterparts, with a minority originating from the measured data and the majority generated through simulation using a linear combination of the Lambert and the Lommel–Seeliger model. This work then presented Lunar SAR to Optical Image U-Net with a Local-Global Attention Module designed to enhance high-frequency feature extraction through parallel processing of spatial details and contextual information. This architecture generates low-incidence-angle optical imagery from SAR observations in lunar polar regions. Quantitative evaluation demonstrates satisfactory structural preservation and perceptual quality in the generated imagery. The resulting low-incidence-angle optical images provide the observational evidence of boulder distributions in crater and subsurface morphological features within PSRs. The method also supports observation of SSRs and heterogeneous remote sensing image registration, offering a new technical pathway for lunar polar exploration.
Opposed Reviewers:	

LunarSAR2O: SAR-to-Optical Image Translation for Permanently Shadowed Region Exploration and its Application

Tong Xia, Niutao Liu*, Yi Zheng, Ya-Qiu Jin

Permanently Shadowed Regions (PSR) at the lunar poles receive no direct sunlight due to the Moon's 1.54° axial tilt, making their study constrained by severe scarcity of optical imagery. Existing ShadowCam optical observations, affected by high-incidence-angle scattered light and topographic blocking, cannot adequately resolve morphological features within Secondary Shadowed Regions (SSR) or rock distributions. While Synthetic Aperture Radar (SAR) can image PSRs independently of illumination conditions and exhibits sensitivity to meter-scale rocks, challenges remain in interpreting its inherent speckle noise patterns and geometric distortions. The study produced the Lunar Optical-SAR Aligned Dataset (LOSAD-14k) containing 14,000 precisely aligned SAR-optical image pairs. The optical images in LOSAD-14k maintain identical incidence geometry with their SAR counterparts, with a minority originating from the measured data and the majority generated through simulation using a linear combination of the Lambert and the Lommel–Seeliger model. This work then presented Lunar SAR to Optical Image U-Net with a Local-Global Attention Module designed to enhance high-frequency feature extraction through parallel processing of spatial details and contextual information. This architecture generates low-incidence-angle optical imagery from SAR observations in lunar polar regions. Quantitative evaluation demonstrates satisfactory structural preservation and perceptual quality in the generated imagery. The resulting low-incidence-angle optical images provide the observational evidence of boulder distributions in crater and subsurface morphological features within PSRs. The method also supports observation of SSRs and heterogeneous remote sensing image registration, offering a new technical pathway for lunar polar exploration.

***Index Terms*— PSR, SAR, LunarS2OUNet, Moon, Optical Images**

1. Introduction

The Moon's axial tilt is 1.54° (Paige et al., 2010). There is no direct solar illumination in some craters near the lunar poles all the year. These areas are referred to as Permanently Shadowed Regions (PSR) (Yin et al., 2024). PSR is attaching global attention but researches about PSR are limited due to the lack of optical images (Bickel et al., 2021). Questions regarding whether the internal morphology of PSR is unique and how to judge the degree of degradation of craters in PSR, remain to be addressed.

The scattered sunlight by nearby elevated terrain is the main lighting source in PSR (Yin et al., 2024). The Narrow Angle Camera (NAC) of Lunar Reconnaissance Orbiter Cameras (LROC) has imaged the interiors of all PSRs which are larger than 20 km², with long-time exposure techniques (Robinson et al., 2010). The resolution ranges from 10 to 20 m/pixel(Brown et al., 2022). The advanced ShadowCam imager onboard the Korea Pathfinder Lunar Orbiter (KPLO), which is specifically designed for PSR imaging (Robinson et al., 2023), acquired optical images with resolution of 1.7 m/pixel. However, images are affected by incidence angle of the scattered light, which made some secondary shadow regions (SSR) still unobservable (Tang et al., 2025; Yin et al., 2024). Additionally, ShadowCam images are not sensitive to rocks with size of meters due to large incidence angle of the scattered light. Therefore, these images cannot be used to determine the craters degradation within the PSR (Fa and Eke, 2018; Fassett et al., 2024).

Impact events, such as meteorite collisions with the lunar surface or volcanic eruptions, may cause the ejection and scattering of rocks. Large boulders are often found around lava tubes and fresh craters. The presence of boulders will influence lander path planning. In addition, the rocks degradation plays a significant role in understanding the evolution of lunar terrain and inferring the age of specific regions. Previous studies have focused solely on high-resolution LROC NAC optical images in low-latitude regions, lacking research on rocks in PSR (Di et al., 2016). Moreover, rocks in PSR are difficult to be detected by using other remote sensing data sources, such as Digital Elevation Model (DEM) (Fassett et al., 2024; Smith et al., 2017).

Synthetic Aperture Radar (SAR) actively emits electromagnetic waves to detect the topography of the lunar poles and does not rely on external light sources. The hybrid-polarized SAR miniature radio frequency (Mini-RF) onboard LRO is designed to detect the PSR of the Moon (Nozette et al., 2010). Since the wavelength of microwave is much longer than that of visible light, SAR is sensitive to rocky areas, roughness, and undulations that are larger than the wavelength. The disadvantages of the current SAR images are the influence of speckle noise and radar geometric distortion, leading to the difficulty in interpretation (Cahill et al., 2014; Campbell et al., 2006; Carrer et al., 2024; Hofgartner and Hand, 2023).

Artificial intelligence proves to be a powerful tool for SAR image interpretation (Bai et al., 2024; Fu et al., 2021; Li et al., 2022; Merkle et al., 2018; Qin et al., 2024). To enhance the interpretability of SAR image, Generative Adversarial Network (GAN) can transform SAR images into optical images that align better with human visual perception (Fu et al., 2021), while traditional

computer vision methods can hardly describe the nonlinear relationships between SAR and optical images. In the field of Earth remote sensing, Fu et al. (Fu et al., 2021) demonstrated that GANs can effectively bridge the nonlinear discrepancies between SAR and optical imagery, generating optical images with high visual quality. Bai et al. (Bai et al., 2024) further indicated that diffusion models significantly enhance the SAR-to-optical (S2O) image conversion process, particularly in image detail reconstruction and noise suppression. Qin et al. (Qin et al., 2024) proposed an enhanced conditional denoising diffusion probabilistic model with spatial frequency refinement to improve high-frequency information generation. However, in planetary science, research on S2O image translation using deep learning remains in its early stages, lacking systematic validation and practical application. Existing S2O translation methods have not adequately accounted for the influence of SAR and optical image registration in image to image conversion, such as geometric distortions, incidence angles, and incidence directions in SAR imagery. Consequently, the absence of high-quality registered datasets poses a challenge for lunar S2O image translation.

This paper introduces Lunar SAR to Optical Image U-Net (LunarS2OUNet), a dedicated network for Lunar S2O image conversion. The study establishes a high-quality co-registered datasets of SAR and optical images to enhance the training effectiveness. The network architecture is specifically designed to capture lunar surface characteristics, enabling simultaneous generation of both large-scale topographic features and small-scale details. A novel Local-Global Attention Module (LGAM) is proposed, employing a dual-branch structure to capture both global contextual information and local high-frequency details, significantly improving the generation quality of key features such as crater edges and rock distributions. The generated optical images effectively suppress speckle noise while maintaining high interpretability. By incorporating SAR images as conditions during both training and inference, the model effectively extracts useful information from SAR data to synthesize optical images with the same incidence geometry of SAR. Evaluation metrics for the generated optical images are validated. Additionally, the synthesized low-incidence-angle optical images of PSRs are compared with ShadowCam optical data to analyze rock distributions and anomalous backscattering regions within small craters. Finally, the generated optical images are utilized to support SAR image registration, providing a promising technical approach for multi-source remote sensing data integration.

The remaining parts of this paper are organized as follows: Section 2 introduces the multi-source remote sensing data, the constructed Lunar Optical-SAR Aligned Dataset (LOSAD-14k), and the proposed LunarS2OUNet architecture with its core modules. Section 3 presents validation of the generated optical imagery quality and stability in non-permanently shadowed regions (non-PSR) at low latitudes, followed by demonstration of the method's capability to generate optical imagery within lunar polar PSRs, with particular focus on the reconstruction of topographic features in SSRs. Section 4 provides comprehensive verification of rock signal in optical and SAR image through simulation alongside multi-source remote sensing data comparison, analyzing the relationship between crater rock distribution characteristics and SAR backscattering intensity, while thoroughly examining the practical application value of generated optical imagery in multi-source remote sensing analysis of lunar craters and SAR image heterogeneous registration. Section 5 gives the conclusions.

2. Data And Method

The overall methodology of this study is illustrated in Fig.1. The process begins with the pixel-level co-registration of mini-RF and DEM data in ArcGIS Pro using a spline transformation model, according to the alignment established in prior work (Nozette et al., 2010; Smith et al., 2017; Xia et al., 2024). Subsequently, optical imagery corresponding to the identical incidence geometry of the mini-RF observations is simulated from the DEM and Kaguya data using a linear combination of the Lambert and the Lommel–Seeliger model (Lohse et al., 2006; McEwen, 1991; Wu et al., 2018). The proposed LunarS2OUNet is then implemented, which incorporates a dedicated data preprocessing module, a deep convolutional network, and a composite loss function. This integrated design serves to improve the detail and visual quality of the synthesized images.

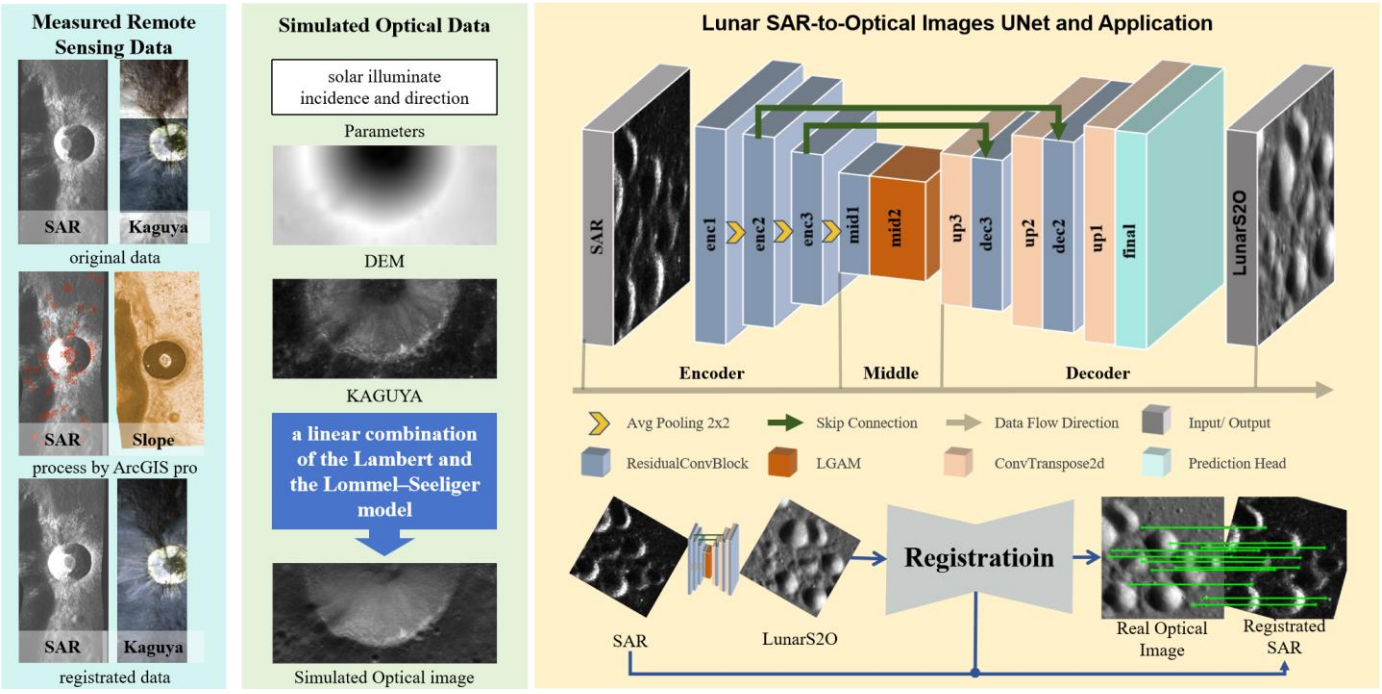

Fig. 1. Overall framework of LunarS2OUNet. The process begins with pixel-level co-registration of multi-source lunar remote sensing data to construct a high-quality dataset. To address the scarcity of well-registered SAR-optical data, a linear combination of the Lambert and the Lommel–Seeliger model was employed to generate simulated optical imagery. The proposed LunarS2OUNet converts SAR images into optical images, which are then used for homologous registration with measured optical images. This registration transformation is subsequently applied to the original SAR data, achieving precise S2O alignment.

2.1 Data and preprocess

This study utilized the following lunar remote sensing datasets, with specifications summarized in Table 1. (1) LROC NAC: Providing a resolution of approximately 1 m/pixel, data from the Lunar Reconnaissance Orbiter (LRO) served as optical training samples (Robinson et al., 2023; Robinson et al., 2010). (2) LROC Wide Angle Camera (WAC): Also from LRO with a resolution of approximately 100 m/pixel, this data was used for lunar surface observation (Speyerer et al., 2011; Wagner et al., 2015). (3) Mini-RF: Operating from LRO, this instrument transmits circular polarization and receives linear polarization with an incidence angle of approximately 49°. The S1 product, representing the total backscattering at 14.8 m spatial resolution, was used for datasets generation and analysis (Nozette et al., 2010). (4) ShadowCam: Data from the KPLO, offering a resolution of about 1.7 m/pixel, was employed for comparative observations of PSRs (Robinson et al., 2023). (5) Kaguya: Multispectral data from the Japan Aerospace Exploration Agency's (JAXA) SELenological and ENgineering Explorer (SELENE) mission, with a resolution of approximately 15 m/pixel, was utilized to simulate optical images (Bussey et al., 2010; Kato et al., 2010). There are 9 bands in Kaguya, but only 415 nm visible band was used (Bussey et al., 2010). Kaguya data, which acquired under near-nadir solar illumination conditions, were employed in the simulation. (6) Lunar Orbiter Laser Altimeter (LOLA) DEM: The data from the LOLA provided detailed topographic data, supporting lunar surface terrain modeling. (7) Special Data Record NAC Digital Terrain Map (SDNDTM): A high-resolution Digital Terrain Model (DTM) (2-4 m/pixel) generated from LROC NAC imagery using photometric stereoscopy. It provides relative elevation information and is constrained by absolute elevations from LOLA, making it essential for the optical image simulations.

Table 1: Specifications of the Lunar Remote-Sensing Datasets

Data product/maps	Mission	Spatial resolution	Source	References	Function
LROC WAC Mosaic	LRO	~100 m	USGS	(Robinson et al., 2010)	Observation
LROC NAC Mosaic	LRO	~1 m	USGS	(Robinson et al., 2010)	Training samples
SDNDTM	LRO	~5 m	USGS	(Smith et al., 2017)	Optical image simulation
Mini-RF Mosaic	LRO	10 - 30 m	USGS	(Nozette et al., 2010)	Training samples, generation
ShadowCam Mosaic	KPLO	~2 m	KARI/USGS	(Robinson et al., 2023)	Comparative observation
Kaguya	SELENE Mission	~15 m	JAXA	(Kato et al., 2010)	Optical image simulation

2.1.1 Data Registration and Mosaic

The datasets used in this study consist of SAR images from Mini-RF and complementary optical imagery. The SAR images, with a spatial resolution of 14.8 m/pixel, inherently contain geometric distortions due to the side-looking imaging geometry (Nozette et al., 2010). To correct for these distortions, the SAR images were co-registered with the reference DEM data at the pixel level using the "Georeference" tool in ArcGIS Pro. This process involved manually adding ground control points to establish precise point-to-point correspondence, followed by the application of a Spline transformation to achieve accurate geometric alignment. Fig. 2a demonstrates the co-registration result between the SAR image and other remote sensing datasets.

The Kaguya optical data, also at 14.8 m/pixel resolution, were registered using the same methodology. Multiple data segments were then mosaicked into a uniform value distribution across the study area. Fig. 2b shows the registered and mosaicked Kaguya data. The SDNDTM data in Fig. 2c with a 4 m/pixel resolution, served as the primary topographic reference for co-registration. A slope map derived from this SDNDTM is presented in Fig. 2d. This study utilized a total of 27 data tracks.

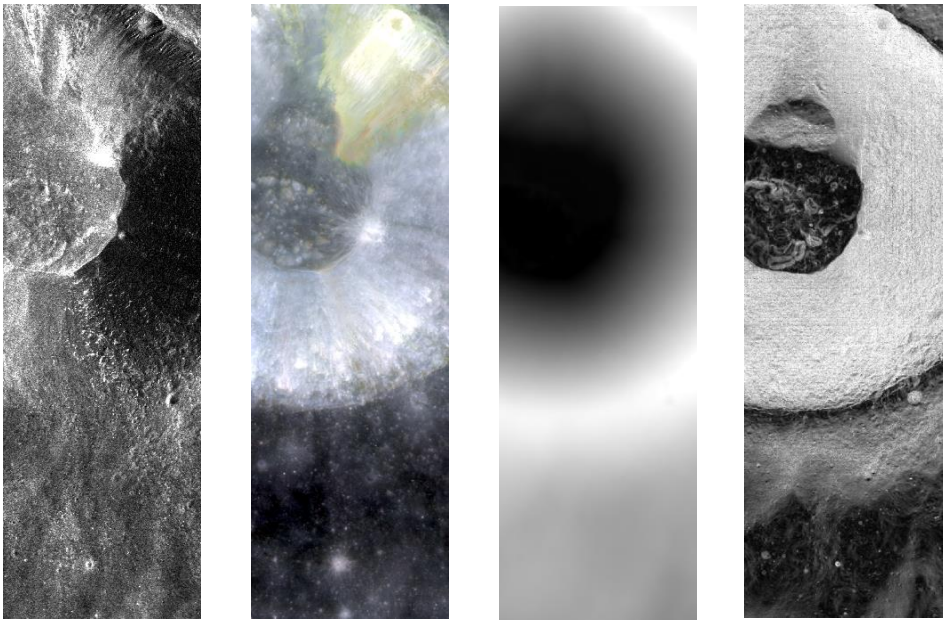

(a) **(b)** **(c)** **(d)**

Fig. 2. Registration Performance of Multi-Source Remote Sensing Data.

2.1.2 Optical Image Simulation

The construction of high-quality training datasets is critical for S2O image translation tasks. In such datasets, SAR images should be free from geometric distortions while optical images must maintain incidence geometry consistent with the SAR data. A significant challenge arises from the limited availability of high-resolution NAC optical images sharing identical incidence geometry with SAR observations. This scarcity of well-aligned data substantially constrains the performance of image generation and style transfer models.

To address this limitation, synthetic optical imagery was generated using a linear combination of the Lambert and the Lommel–Seeliger model. Based on the lunar surface reflectance model (McEwen, 1991), this approach incorporates the incidence geometry parameters of SAR images along with high-resolution DEM topographic data and Kaguya multispectral data to produce optical imagery with arbitrary incidence and illumination angles. The simulation process explicitly accounts for key factors in lunar reflectance characteristics, including solar irradiance, albedo distribution, and topographic slopes. The constructed datasets comprise two components, a limited set of real LROC NAC images serving as reference benchmarks, supplemented by extensive simulated optical imagery with incidence geometry matching SAR observation parameters.

The intensity reflected from lunar surface is written as (Yin et al., 2024):

$$I = \frac{TSI \times S_0 \times \cos(\theta_i) \times A \times G(\theta_i, \theta_e)}{\cos(\theta_t)} \tag{1}$$

where TSI is the total solar irradiance. TSI is treated as a constant and thus neglected in the following analysis. A is albedo data from Kaguya data, with a wavelength of 414 nm (Kato et al., 2010). $G(\theta_i, \theta_e)$ is the direction function of the reflection. θ_i is the solar incidence angle, θ_e is the angel between the line of the viewer and the normal, and θ_t is the angle of the slope, which can be seen in Fig. 3. $\cos(\theta_i)$ is used to model the solar irradiance on each slope while $\cos(\theta_t)$ is used to calculate the area of the tilted

slope. The area of each slope is $S_t = S_0 / \cos(\theta_t)$, where the area S_0 of each slope projected on the horizontal plane is constant. The constant S_0 is ignored in calculation. There are no topographic occlusion in simulation.

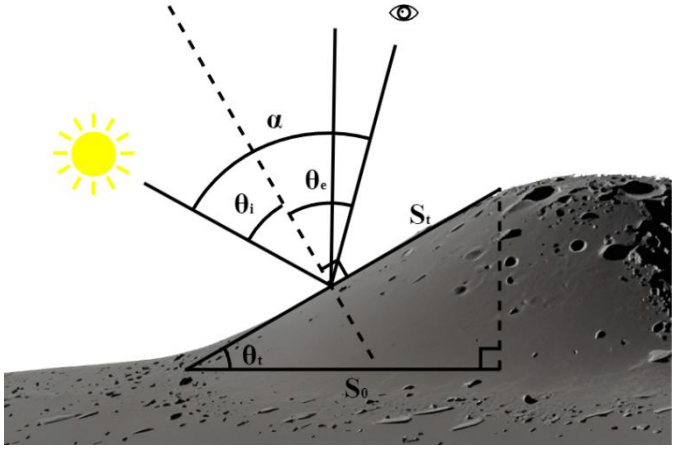

Fig. 3. Conceptual illustration. The relationship between the sun, the lunar surface, and the viewer.

A linear combination of the Lambert and the Lommel–Seeliger model used in simulation is (Lohse et al., 2006; McEwen, 1991; Wu et al., 2018):

$$G(\theta_i, \theta_e) = (1-\omega)\cos(\theta_i) + 2\omega \times \frac{\cos(\theta_i)}{\cos(\theta_i) + \cos(\theta_e)} \quad (2)$$

where ω is a function of the phase angle α (i.e., the angle between the sunlight and the line of the viewer) (Lohse et al., 2006):

$$\omega = 1 - 0.019\alpha + 0.242 \times 10^{-3}\alpha^2 - 1.46 \times 10^{-6}\alpha^3 \quad (3)$$

The study uses LunarS2OUNet to generate optical images from SAR images, preserving the sensitivity of SAR images to rocks and allowing observation of rock distribution. The style of the generated optical images is consistent with that of low-latitude optical images at small illumination angles, which is bright. In addition, the distribution of rocks can be observed under small solar illumination angles, and cannot under large ones.

This study selects fresh crater at (8.74°N, 33.19°E) for illustration. Kaguya data with a resolution of 14.8 m/pixel of this area were used as the albedo A in Equation 1. The Kaguya data utilized in this study were acquired under near-nadir solar illumination conditions. DTM data with a resolution of 2 m/pixel were used for modeling the 3D morphology. The viewer observes the lunar surface at nadir point in the simulation.

Optical images under different solar illumination angles were simulated, as shown in Fig. 4. Figs. 4a-c are measured LROC NAC optical images with a resolution of 1 m/pixel, and incident angles of 16.70°, 41.67°, and 69.68°, respectively.

In Figs. 4a and b, the rock ejecta blankets are bright in the surrounding lunar regolith. In Fig. 4c, the optical image cannot distinguish between rock and lunar regolith. The generated optical images are shown in Figs. 4d-f. The simulated optical images are consistent with the measured optical images, validating the reliability of the simulation.

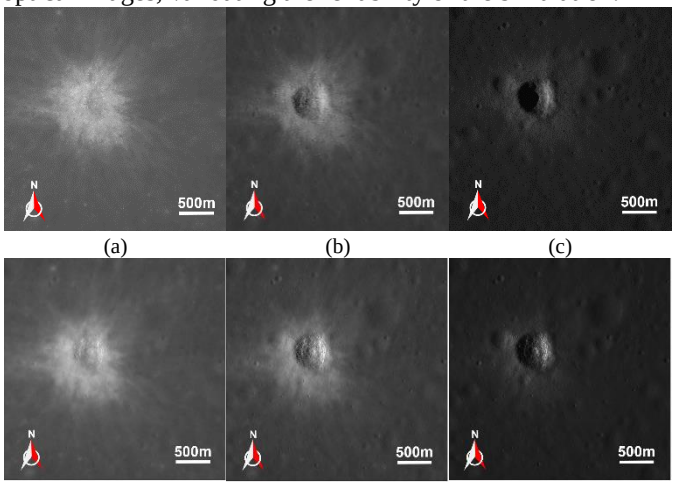

Fig. 4. Optical images from LROC NAC and the corresponding simulation. (a-c) The high-resolution LROC NAC optical images (M188021351, M1236388169, M1218738444) with a resolution of 1.00 m/pixel, centered at the coordinates of the crater (8.74°N, 33.19°E). The illumination angles for Figs. a-c are 16.7°, 41.67

°, and 69.68°, respectively. (d-f) The optical images simulated from a linear combination of the Lambert and the Lommel–Seeliger model by DTM data (MIA_3C5_03_02326N089E0334SC) and Kaguya data (NAC_DTM_TRANQPIT1_E084N0332).

To validate the simulated optical images in Fig.4, comparative evaluation against measured optical imagery was conducted using quantitative metrics including Peak Signal-to-Noise Ratio (PSNR) (Eskicioglu and Fisher, 1995), Structural Similarity Index (SSIM) (Wang et al., 2004), and Learned Perceptual Image Patch Similarity (LPIPS) (Zhang et al., 2018) in Table 2. For the SSIM metric, higher values indicate greater structural similarity. The PSNR metric with higher values representing better signal-to-noise ratio. Conversely, lower LPIPS scores reflect closer perceptual similarity to the reference imagery. The average results indicate a PSNR of 26.45 dB, SSIM of 0.85, and LPIPS of 0.05 between the simulated and measured optical images. According to the perception-consistent metric proposed by Zhang et al. (Zhang et al., 2018), LPIPS scores below 0.05 generally indicate excellent perceptual quality. The achieved value of 0.05 approaches this threshold, demonstrating favorable characteristics in terms of human visual perception. In the field of image generation and restoration, PSNR exceeding 28 dB and SSIM above 0.85 are typically regarded as competitive performance levels (Zhou et al., 2004). The obtained results, where PSNR is 26.45 dB and SSIM is 0.85, approach these benchmarks. It should be noted that lunar optical image simulation presents considerably higher complexity compared to conventional image restoration tasks, as it requires simultaneous modeling processes and adaptation to complex terrain and lunar surface geology. Within this context, the quantitative evaluation results validate the reliability of the simulation approach and establish a solid foundation for subsequent S2O image translation research.

Table 2. Reliability Metrics of Simulated Images in Fig. 4 across Different Incidence Angles

Different Incidence angle	16.70°	41.67°	69.68°	Average Value
SSIM	0.87	0.80	0.87	**0.85**
PSNR	27.41 dB	25.27 dB	26.67 dB	**26.45 dB**
LPIPS	0.04	0.06	0.05	**0.05**

2.1.3 LOSAD-14k Datasets

Through co-registration by ArcGIS Pro, 25 SAR-measured optical-simulated image pairs and 2 SAR-measured optical-measured image pairs were generated. These image pairs were cropped to produce 2,500 base samples, which were subsequently expanded to 14,460 samples through data augmentation techniques. All data were standardized to a spatial resolution of 14.8 m/pixel.

The LOSAD-14k was constructed with this material. The images in LOSAD-14k undergo meticulous geometric correction to ensure the elimination of distortions in SAR data and maintain perfect incidence angle and direction consistency between optical and SAR images. The datasets comprise 12,006 training sample pairs, 1,074 validation sample pairs, and 1,380 test sample pairs. The datasets encompasses characteristic lunar terrains including Maria and highlands, with sample pairs in multiple pixel dimensions (256×256, 512×512, and 1024×1024). For compatibility with deep learning architectures, all images were resized to 256×256 pixels during training. In the preprocessing stage, input images were converted to tensor format and normalized to comply with standard model training protocols.

2.2 Lunar SAR to Optical Image U-Net

2.2.1 Network Architecture Design

To address the challenges of terrain complexity and detail features in lunar S2O image translation, the dedicated LunarS2OUNet is designed, as illustrated in Fig. 1. Based on an encoder-decoder structure, the network integrates deep residual connections and attention mechanisms to achieve collaborative modeling of large-scale terrain features and small-scale details (He et al., 2015).

The encoder section employs a three-stage residual convolutional block for feature extraction, with each stage performing double downsampling to expand the receptive field and doubling the number of channels (64→128→256) (He et al., 2015). This design captures global topographic contours while preserving essential spatial information.

The intermediate layer consists of residual blocks and a Local-Global Attention Module (LGAM), augmented by a Pyramid Pooling module for multi-scale feature fusion (Zhao et al., 2017). This structure captures multi-level contextual information through four pooling windows of sizes [1, 2, 4, 8], followed by a 1×1 convolution that compresses the fused 1280-dimensional features to 256 dimensions, effectively balancing computational efficiency and feature representation capability.

The decoder section utilizes ConvTranspose2d for upsampling and incorporates skip connections to concatenate features from corresponding encoder levels with decoded features, ensuring effective transmission of detail information (Ronneberger et al., 2015). The final output is generated through a 3×3 convolution and Sigmoid activation, producing three-channel optical imagery.

Compared to traditional general-purpose image translation models such as CycleGAN (Zhu et al., 2017), Pix2Pix (Isola et al., 2017) , and Diffusion models (Ho et al., 2020), this network is specifically optimized for lunar terrain characteristics. While maintaining the advantages of the U-Net baseline framework, the LGAM significantly enhances detail reconstruction capability under complex terrain conditions.

2.2.2 LGAM

Conventional channel attention mechanisms, such as the Squeeze-and-Excitation (SE) module (Hu et al., 2017), typically employ global average pooling to aggregate spatial information. While effective in capturing global contextual dependencies, this approach tends to overly smooth high-frequency details, which are particularly critical for representing fine lunar surface features like crater walls and small-scale textures. To address this limitation and enhance the network's capacity to preserve both global structures and local details, a LGAM in Fig. 5 is proposed.

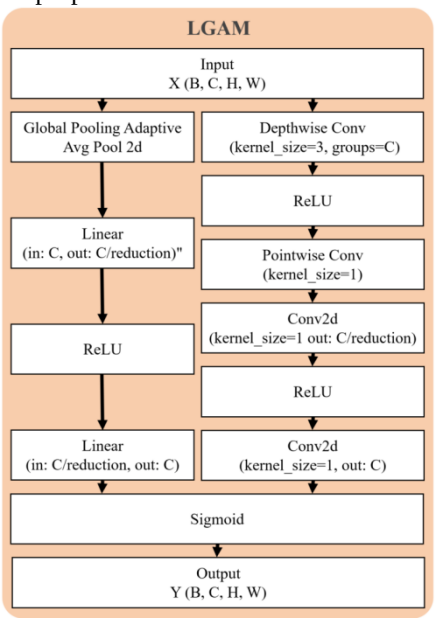

Fig. 5. Structure of the LGAM. the global branch employs an SE module to capture holistic semantics, while the local branch uses depthwise separable convolutions to preserve high-frequency details. The two branches are fused via weighted summation to achieve adaptive channel recalibration.

Given the input feature map $X \in \mathbb{R}^{B\times C\times H\times W}$, the LGAM generates an adaptive attention map Y by combining outputs from the global and local branches.

The global branch on left side in Fig. 5 captures long-range semantic correlations via global average pooling followed by two fully connected layers (Hu et al., 2017):

$$y_{global} = W_2\delta(W_1 GAP(x)) \tag{4}$$

where $GAP(x) \in \mathbb{R}^{B\times C}$ is global average pooling, $W_1 \in \mathbb{R}^{\frac{C}{r}\times C}$ and $W_2 \in \mathbb{R}^{C\times\frac{C}{r}}$ are learnable parameters, r is reduction ratio, and $\delta(\cdot)$ denotes the ReLU activation. After reshaping, $y_{\text{global}} \in \mathbb{R}^{B\times C\times 1\times 1}$.

The local branch on right side in Fig. 5 enhances high-frequency spatial information using a depthwise separable convolution, followed by lightweight channel compression and excitation:

$$f_{local} = Conv_{1\times1}(\delta(DWConv_{k\times k}(x))) \tag{5}$$

Then, channel-wise modulation is performed through two pointwise convolutions:

$$y_{local} = Conv_{1\times1}(\delta(Conv_{1\times1}(f_{local}))) \tag{6}$$

where $DWConv_{k\times k}$ represents depthwise convolution, k = 3 and $\text{Conv}_{1\times1}$ denotes pointwise convolution.

Here, $y_{\text{local}} \in \mathbb{R}^{B\times C\times H\times W}$, retaining spatial structure without global pooling.

The outputs from the two branches are fused via element-wise summation and passed through a Sigmoid activation:

$$Y = \sigma(y_{global} + y_{local}) \tag{7}$$

where $\sigma(\cdot)$ denotes the sigmoid activation.

The final modulated output is obtained by channel-wise and spatially reweighting the input features (Hu et al., 2017):

$$X_{out} = X \odot Y \tag{8}$$

where $\odot$ denotes element-wise multiplication with broadcasting between the two attention maps.

This design enables LGAM to simultaneously capture global contextual cues through the pooling pathway and local spatial variations through depthwise convolutions. The adaptive fusion of these two signals allows the network to selectively emphasize texture-rich regions such as crater rims, small depressions, and surface ridges, while preserving global illumination and terrain consistency. As a result, LGAM effectively mitigates detail degradation in conventional SE modules and enhances the perceptual realism of the generated optical images.

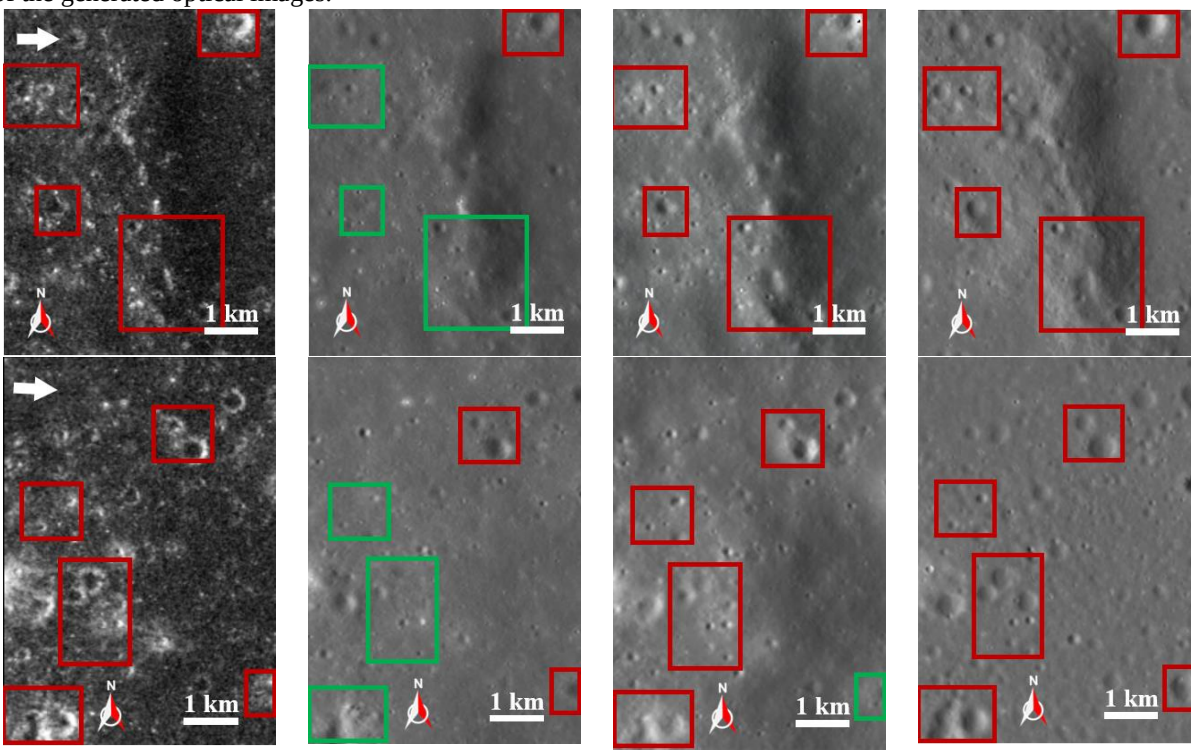

(a) (b) (c) (d)

Fig. 6. Comparison of S2O image translation results. (a) Input SAR image. (b) Optical image generated by conventional SE module. (c) Result generated using the proposed LGAM module. (d) Ground Truth. Regions of higher fidelity are marked with red boxes, while areas containing noticeable artifacts are indicated by green boxes.

A comparative visualization of the generated results is presented in Fig. 6. Fig. 6a shows the input SAR image, Fig. 6b displays the optical image generated using the SE module, Fig. 6c presents the result obtained with the proposed LGAM, and Fig. 6d provides the ground truth. In both Figs. 6b and c, regions of higher fidelity are highlighted in red boxes, while areas with noticeable artifacts are indicated in green boxes. Compared to the conventional SE structure, the images generated with the LGAM exhibit more complete reconstruction of high-frequency details such as craters and depressions, as visible in the red-boxed areas of Fig. 6c. Furthermore, the LGAM results demonstrate clearer textural variations in terrain relief, indicating a superior ability to recover high-frequency information.

Experimental results confirm that the LGAM module maintains high detail fidelity under complex terrain and varying illumination conditions, leading to a marked improvement in both visual quality and interpretability of the generated imagery. However, the current network demonstrates heightened sensitivity to high-frequency information, which may introduce artificial undulations even in flat terrain areas. As observed in Fig. 6c, certain flat regions exhibit shadow-like protrusions not present in the reference image in Fig. 6d, potentially resulting from excessive enhancement of high-frequency features. While LGAM effectively enhances detail preservation, it tends to introduce artifacts in texture-sparse regions. Subsequent improvements could incorporate adaptive weight modulation mechanisms to optimize high-frequency gain, suppressing anomalous responses in flat areas. Such adjustments would maintain detail enhancement while reducing false positive rates, thereby improving overall generation stability.

2.2.3 Joint Loss Function Design

To ensure comprehensive quality of the generated images in terms of structure, texture, and perceptual fidelity, a multi-term joint loss function is formulated as follows:

$$L_{total} = L_{GAN} + \lambda_1 L_{pixel} + \lambda_2 L_{perceptual} + \lambda_3 L_{hist} + \lambda_4 L_{TV} \quad (9)$$

where L_{GAN} is employed to enforce distributional consistency between the generated and real optical images via a discriminator network, thereby enhancing the visual realism of the outputs and preventing excessive smoothing or blurring (Goodfellow et al., 2014). L_{pixel} is the Smooth L1 loss constrains pixel-wise discrepancies between the generated and target images, ensuring that principal structures in the SAR image are spatially aligned with those in the synthesized optical image (Girshick, 2015). $L_{perceptual}$, *which* based on high-level semantic features extracted from a pre-trained VGG network, quantifies perceptual differences between the generated and reference images, effectively improving overall visual quality and semantic coherence (Johnson et al., 2016). L_{hist} encourages the generated images to exhibit tonal and contrast characteristics closer to those of real lunar optical imagery by aligning the cumulative histograms of luminance and color distributions (Ulyanov et al., 2016). L_{TV} suppresses high-frequency noise and unnatural artifacts in the generated images, enhancing spatial smoothness and adherence to the continuous variations typical of natural images (Mahendran and Vedaldi, 2014; Rudin et al., 1992). The study determined the values of hyperparameters λ_1-λ_4 through weight sensitivity experiments. The hyperparameters were set as $\lambda_1 = 10$, $\lambda_2 = 5$, $\lambda_3 = 1$, and $\lambda_4 = 0.1$ to balance the influence of each loss term during training.

Ablation studies were conducted to evaluate the effectiveness and necessity of each loss component (Isola et al., 2017; Wang et al., 2018), with results summarized in Table 3. The experiments demonstrate that removing the $\boldsymbol{L_{Perceptual}}$ deteriorates the LPIPS metric to 0.33, confirming its critical role in preserving perceptual quality. Eliminating the L_{pixel} reduces PSNR by approximately 1 dB, indicating its fundamental contribution to spatial accuracy. Although the absence of L_{hist} and L_{TV} yields marginal SSIM improvement, this occurs alongside degradation in other metrics, suggesting their supplementary role in optimization. All loss terms play complementary roles, where the absence of any component leads to performance degradation in specific aspects. The joint loss function effectively balances structural accuracy and visual quality by integrating supervision signals at multiple levels, confirming the rationality of its design and the stability of the training process.

Table 3. Ablation Study on the Effectiveness and Necessity of Each Loss Component.

Variant	$L_{perceptual}$	L_{hist}	L_{TV}	L_{pixel}	PSNR↑	SSIM↑	LPIPS↓
full_model	√	√	√	√	**26.67 dB**	**0.8279**	**0.26**
- $L_{perceptual}$	×	√	√	√	25.15 dB	0.8083	0.33
- L_{hist}	√	×	√	√	26.39 dB	**0.8290**↑	0.29
- L_{TV}	√	√	×	√	25.58 dB	**0.8361**↑	0.28
- L_{pixel}	√	√	√	×	25.64 dB	**0.8326**↑	0.28

In the ablation study of the joint loss function, the removal of certain loss components resulted in little improvements in the SSIM metric, a phenomenon that requires careful analysis through the lens of SSIM's evaluation mechanism. As a structural similarity measure, SSIM exhibits specific sensitivity to variations in luminance, contrast, and structural information (Wang et al., 2004). Experimental data indicate that when $L_{histogram}$, L_{TV}, or L_{pixel} loss are individually removed, SSIM values show increases ranging from 0.0011 to 0.0082, reflecting the complex interactions among loss components.

However, these SSIM improvements consistently coincide with significant degradation in both PSNR and LPIPS, where 0.28-1.52 dB decrease and 0.02-0.07 increase, respectively. This relationship clearly demonstrates that isolated improvement in SSIM fails to comprehensively represent the actual changes in generation quality. This phenomenon indicates the necessity of employing a multi-dimensional evaluation framework. In the design of joint loss functions, systematic balancing of interactions between different loss components is essential to maintain structural similarity while preserving both pixel-level accuracy and perceptual quality, ultimately achieving comprehensive enhancement of generation performance.

The training process uses the Adam optimizer, with generator and discriminator learning rates set to 0.0002 and 0.0001, respectively, and a batch size of 8. Mixed-precision training and gradient clipping techniques are employed to accelerate convergence.

3. RESULT

3.1 Multi-class Terrain Generation

To systematically evaluate the performance of the generated images in typical lunar terrain, four representative non-PSR morphologies were selected for validation, pan-like craters, bowl-like craters, undulated terrain with crater clusters, and flat areas (Wagner et al., 2015). The selected regions are located at (1.29°S, 148.29°W), (17.95°S, 34.98°E), (33.67°N, 40.21°W), and (17.58 °S, 26.78°E), respectively.

In the generated optical images, the solar illumination direction aligns with the SAR observation geometry. Slopes facing the radar appear brighter while those facing away appear darker, corresponding to the "sun-facing slopes are bright, shadowed slopes

are dark" characteristic in measured optical imagery (Fa and Cai, 2013; Liu and Jin, 2023). Fig. 7 presents a comparative analysis of four different methods across these regions. The first column shows Mini-RF SAR images at 14.8 m/pixel resolution with approximately 49° incidence angle, with white arrows indicating the radar illumination direction (Nozette et al., 2010). The second column displays CycleGAN results, which avoid cross-domain registration issues but exhibit noticeable tonal distortion and granular noise (Zhu et al., 2017). The third column presents Pix2Pix outputs, demonstrating limited capability in establishing effective S2O mapping relationships (Isola et al., 2017). The fourth column shows Diffusion Model results, showing sensitivity to SAR noise and tendency to generate artificial details (Ho et al., 2020). The fifth column contains the proposed LunarS2OUnet results, which maintain structural information from SAR images while achieving optimal visual quality. The sixth column display the 49° simulated optical images, replicating the lighting conditions in non PSRs by direct solar light.

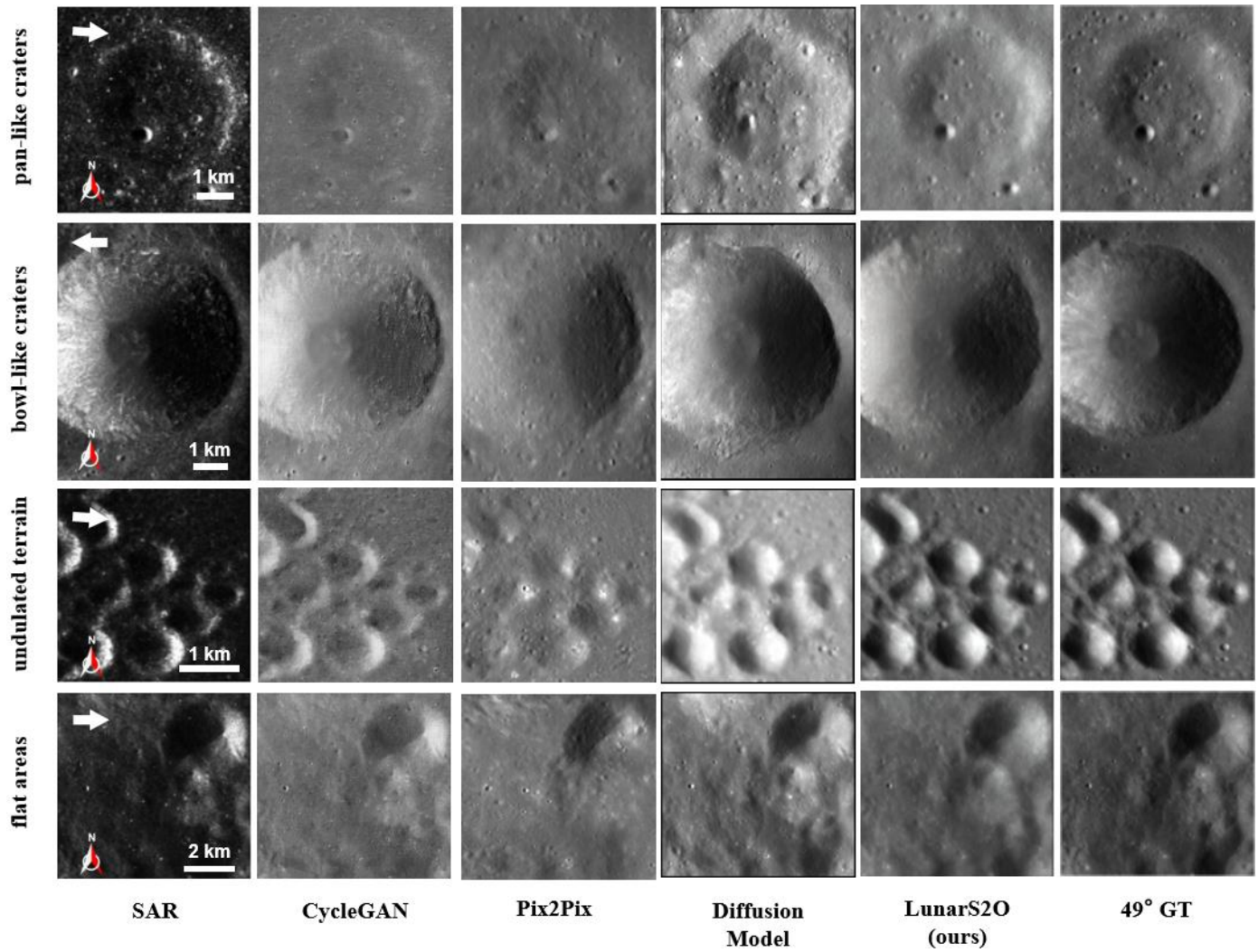

Fig. 7. Comparative analysis of S2O image translation performance across forth methodologies. From left to right, Mini-RF SAR imagery at 14.8 m/pixel resolution and 49° incidence angle, with radar illumination direction indicated by arrows. CycleGAN results exhibiting tonal distortion and granular noise. Pix2Pix outputs demonstrating limited cross-domain mapping capability. Diffusion Model results showing noise sensitivity and artificial detail generation. Proposed LunarS2OUnet results maintaining structural integrity with optimized visual quality. Simulated optical references at 47° incidence angle representing lighting conditions in non-PSR. The first row displays pan-like craters. The second row presents bowl-like craters. The third row shows undulated terrain with crater clusters, and the fourth row comprises relatively flat areas.

Experimental results indicate that existing methods exhibit significant limitations. CycleGAN, while preserving detail features through its 9-residual-block architecture, exhibits limitations in maintaining space consistency and suppressing noise. The generated images typically display noticeable granular noise and insufficient surface texture smoothness, failing to effectively eliminate inherent speckle noise from SAR imagery. Pix2Pix demonstrates insufficient capability in learning cross-domain feature mappings. The network fails to adequately capture terrain elevation variation information from SAR data and shows limited expressiveness for critical structural features, resulting in generated optical images that lack essential topographic details. Diffusion Models, despite producing partially plausible details, exhibit pronounced stability issues. The generated results show considerable variations in luminance and tonal characteristics, while certain output features remain inconsistent with the structural information

present in the original SAR data, ultimately failing to achieve complete and accurate terrain reconstruction. Comparatively, LunarS2OUnet accurately preserves topographic structures from SAR data while demonstrating superior performance in color fidelity and detail authenticity.

To further evaluate the stability of the generation network, consistency analysis was performed on the results derived from SAR images of the same region with different observation directions. Two Mini-RF SAR datasets acquired at different times over a typical area near the lunar south pole were selected for testing, with the following identifiers, LSZ_04587_2S1_OKU_87S089_V1 and LSZ_04611_2S1_OKU_82S089_V1 in Fig. 8a and b. These datasets cover the same geographical area but differ in imaging geometry and acquisition time (Nozette et al., 2010).

Fig. 8 presents the two SAR datasets along with their corresponding generated optical images. Despite variations in viewing angle and acquisition time among the input data, the LunarS2O images in Fig. 8c and d exhibit strong consistency in crater morphology, spatial structure, and textural characteristics. Key topographic elements such as crater morphology and topographic structure are consistently represented across the generated results.

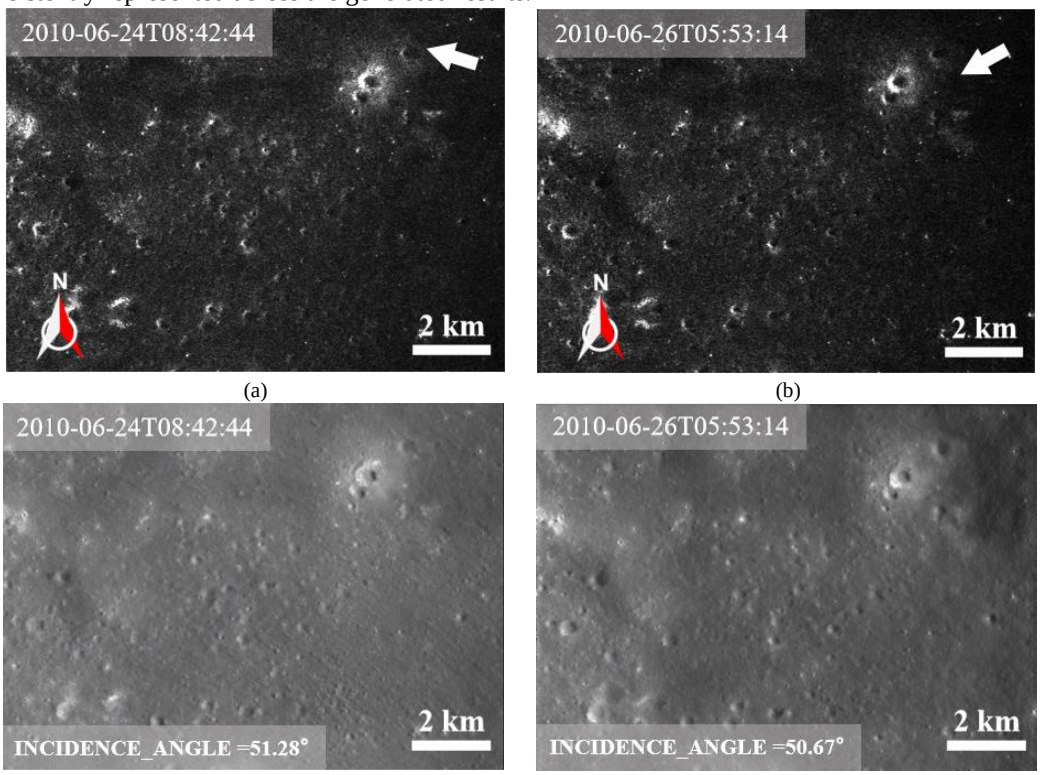

Fig. 8. Consistency validation of SAR image generation results. (a) SAR image centered at (-88.26°, 44.66°) with illumination direction indicated by white arrow and incidence angle of 51.28°. (b) SAR image of the same region acquired at different time with incidence angle of 50.67°. (c) LunarS2O image generated from Fig. a. (d) LunarS2O image generated from Fig. (b). Data sources, LSZ_04587_2S1_OKU_87S089_V1 and LSZ_04611_2S1_OKU_82S089_V1.

This cross-direction consistency demonstrates the robustness of LunarS2OUNet in extracting terrain features from SAR images, with minimal influence from variations in observation geometry. The method reliably produces optical image outputs from SAR data acquired at different directions, confirming the stability and practical applicability of the network model.

Although the generated images achieve 14.8 m/pixel resolution, some small craters remain undetected compared to measured optical imagery due to limitations in the original SAR data resolution. Future missions such as Chang'e-7 could potentially acquire higher-resolution SAR data, which may enable the generation of improved optical images (Wang et al., 2024b).

3.2 LunarS2O in PSR

PSRs have become key targets for lunar exploration due to their unique illumination conditions and potential water-ice deposits (Wang et al., 2024b). Acquiring complete and continuous optical imagery is crucial for future missions such as lunar base construction and the Chang'e-7 mission. Conventional optical imaging which is constrained by lighting conditions, cannot achieve comprehensive low-incidence-angle optical coverage of PSRs (Robinson et al., 2023; Robinson et al., 2010). The LunarS2O method presented in this study offers an effective solution to this challenge through the generation of low-incidence-angle optical images of PSRs.

Fig. 9 shows a comparison of multi-source remote sensing data near the candidate landing area for the Chang'e-7 mission (Wang et al., 2024b; Zhong et al., 2025). The red star indicates the region near the potential candidate landing area, and the blue line

delineate PSR boundary (Mazarico et al., 2011). Fig. 9a shows the SAR image of this region, while Fig. 9b displays the optical image formed by merging LROC WAC and ShadowCam data (Robinson et al., 2023; Robinson et al., 2010), which exhibits noticeable data gaps and discontinuities. In contrast, the LunarS2O image in Fig. 9c provides continuous coverage. It completely represents the topographic variations and crater distributions from the landing site to PSR areas, offering reliable reference for path planning and navigation tasks.

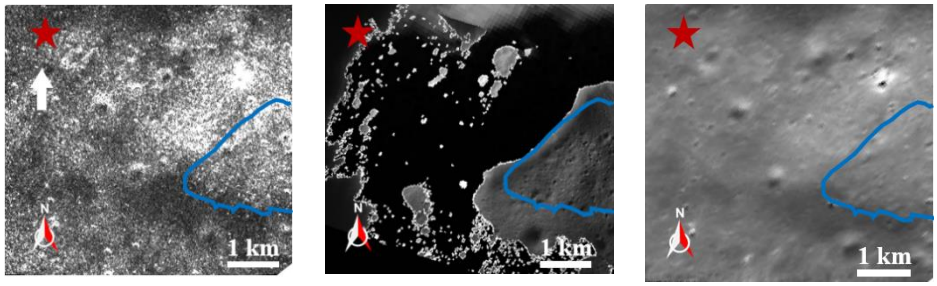

(a) (b) (c)

Fig. 9. Comparison of multi-source remote sensing images in the potential Chang'e-7 candidate landing area (Zhong et al., 2025). (a) SAR image. (b) fused LROC WAC and ShadowCam optical image with data discontinuities. (c) LunarS2O image achieving complete optical coverage. Red star is region near the Chang'e-7 mission landing site. Blue line is PSR boundary.

The crater in Fig. 10 locates at (88.72°S, 169.08°E) in the lunar south polar. Fig.10a shows the optical image acquired by LROC WAC and NAC, with approximately 20 m/pixel resolution and an incidence angle of about 70° (Brown et al., 2022; Robinson et al., 2010; Yin et al., 2024), showing noticeable stitching artifacts and abrupt brightness changes. Fig.10b presents the high-resolution ShadowCam image, with approximately 1.9 m/pixel resolution and an incidence angle of about 70° (Robinson et al., 2023), where significant shadowing occurs due to topographic blocking and high incidence angles. Fig. 10c displays the low-incidence-angle optical image generated by LunarS2OUNet, with 14.8 m/pixel resolution and 49° incidence angle. It completely represents the crater morphology and distribution and maintains optical characteristics consistent with natural low-incidence-angle illumination. The image provides complete and continuous coverage without the noticeable stitching artifacts present in ShadowCam and LROC NAC optical data. The LunarS2O image demonstrates particular sensitivity to boulder distributions on crater walls, where brighter areas are identified as rockfall.

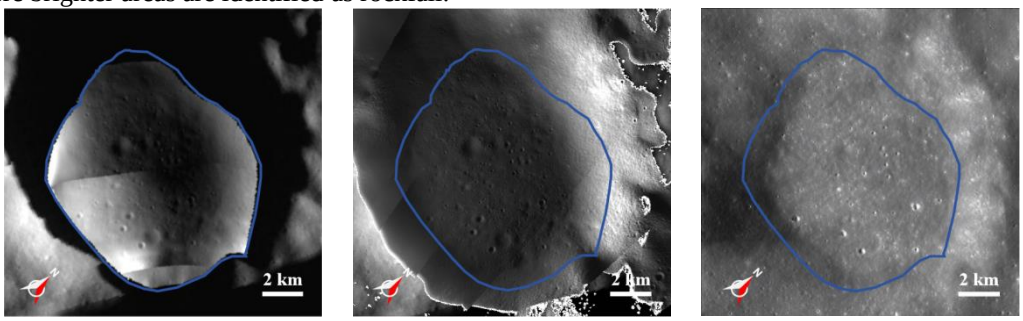

(a) (b) (c)

Fig. 10. Multi-source data comparison of Faustini crater. (a) NAC optical image with ~20 m/pixel resolution, ~70° incidence angle. (b) ShadowCam high-resolution image with ~1.9 m/pixel resolution, ~70° incidence angle. (c) LunarS2O image with ~14.8 m/pixel resolution, ~49° incidence angle. The LunarS2O imagery typically displays low-latitude optical characteristics. The measured optical images appear brighter at lower latitudes and darker at higher latitudes. Blue line is PSR boundary.

The generated images effectively suppress noise interference while preserving the sensitivity of SAR data to rock distributions. Fig. 11 provides a detailed comparison in Faustini crater. In the SAR image in Fig. 11a, fresh craters with rocky ejecta blankets, marked by red circle, contrast distinctly with craters without ejecta blankets, marked by white circle. The ejecta blanket surrounding a crater can be used to determine the degradation of craters (Fa and Eke, 2018). The ShadowCam image in Fig. 11b exhibits low brightness due to high incidence angle limitations, making rock distributions difficult to identify. The LunarS2O image in Fig. 11c significantly improves the discernibility of lunar surface morphology while maintaining incidence geometry consistent with SAR, providing important evidence for analyzing crater degradation states. The length and direction of the ejecta blanket in SAR images can be used to infer the impact direction and angle of the meteorite (Bray et al., 2008; Herrick and Forsberg-Taylor, 2003; Kaydash et al., 2014).

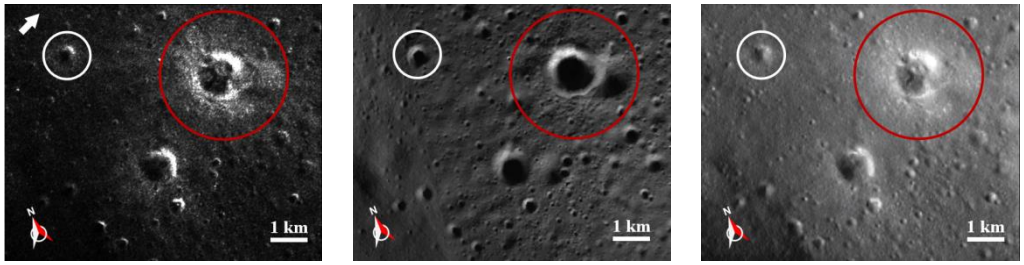

(a) (b) (c)

Fig. 11. Detailed comparison of rock distribution characteristics. (a) SAR image with red circle marking fresh craters with rocky ejecta blankets and white circle marking craters without ejecta blankets. (b) ShadowCam optical image. (c) LunarS2O image.

To validate the accuracy of the rocky ejecta blanket in the generated optical images, this study conducted simulations using optical and SAR methods in the following section.

3.3 Secondary Shadow Region

In the study of optical imaging within PSRs, SSRs refer to sub-regions of PSRs that cannot be reached by first-order scattered light at the time of observation (Carruba and Coradini, 1999). Since the incidence angle of scattered light within PSRs typically exceeds 70° (Yin et al., 2024), SSRs are primarily distributed in areas such as crater floors where direct scattered illumination is minimal (Carruba and Coradini, 1999). Conventional long-exposure optical imaging techniques, constrained by the high incidence angles, cannot effectively observe the internal morphology of SSRs. In contrast, SAR imaging, with its smaller incidence angle of approximately 49°, penetrates shadowed areas to acquire topographic information of SSRs. The detection and study of SSRs hold significant scientific value due to the fact that their low-temperature environments are more conducive to preserve volatile substances. Furthermore, future lunar in-situ exploration missions require the identification and avoidance of SSRs to ensure operational safety.

Figs. 12a-c present observational results of the largest crater within the Faustini crater (87.22°S, 75.94°E), which is named Malinkin (Tye et al., 2015). This bowl-shaped crater has a diameter of 8.28 km. In Fig. 12a, the SAR image includes a white arrow indicating the radar illumination direction. Fig. 12b, the ShadowCam optical image, shows extensive SSRs due to topographic obstruction and visible stitching artifacts in the left corner. Fig. 12c, the LunarS2O image, maintains the same incidence geometry as the SAR data, effectively reduces shadowed areas due to different incidence geometry, and clearly reveals the texture of rock distributions on the crater wall and the morphology of the crater floor. Small craters and wall textures within shadowed areas, not observable in the ShadowCam image, are visible in the generated image. The bright areas on the crater wall are identified as rockfall deposits. Three distinct rockfall traces, indicated by red arrows in Fig. 12c, are identified in areas originally obscured by shadows in Fig. 12b. Additionally, an isolated crater near the floor of Malinkin crater is documented in red circle 1, along with a cluster of densely distributed craters along the interior rim of Malinkin crater in red circle 2. These features, previously undetectable in the ShadowCam image, are clearly resolved in the LunarS2O imagery. Combined with the absence of an external ejecta blanket, these characteristics indicate the crater is in a moderate state of degradation.

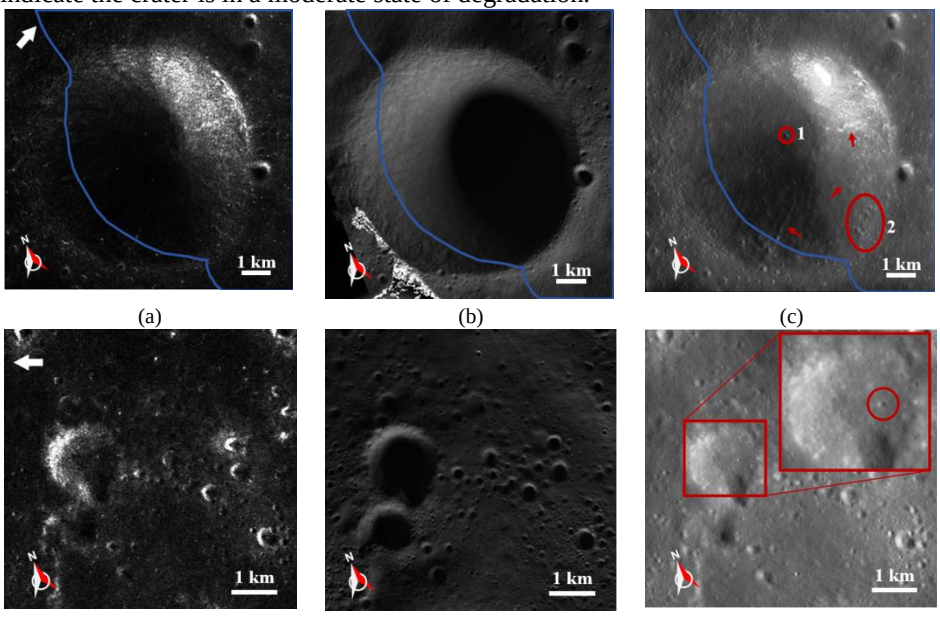

(a) (b) (c)

(d) (e) (f)

Fig. 12. Multi-scale analysis of craters within Faustini crater region. (a-c) Malinkin crater (87.22°S, 75.94°E). (a) SAR image (7.5 m/pixel) with white arrow indicates radar illumination direction. (b) ShadowCam image showing SSRs and stitching artifacts. (c) LunarS2O image revealing rockfall distributions and floor morphology. (d-f) Floor crater (87.12°S, 85.28°E). (d) SAR image with speckle noise. (e) ShadowCam image exhibiting SSRs. (f) LunarS2O image identifying small crater (red circle) and rockfall textures (red box). Blue line indicates PSR boundary.

A detailed analysis of a typical SSR on the floor of the Faustini crater (87.12°S, 85.28°E) in Figs. 12d-f. The SAR image in Fig. 12d is difficult to interpret due to noise interference. The ShadowCam image in Fig. 12e exhibits significant shadowing caused by the high incidence angle of scattered light and topographic blocking. The LunarS2O image in Fig. 12f reveals the crater's floor morphology, identifying a small crater in red circle and distinct rockfall textures on the crater wall in red box. This enhancement enables assessment of crater depth and interior rock distribution. Shadowing previously obscured approximately 90% of the crater floor area in the red box crater, which has been completely eliminated in the LunarS2O image. SSRs have been fully lighted in 65 craters exceeding 0.15 km in diameter, as demonstrated in Fig. 12f. These results provide information for terrain risk assessment and path planning in future lunar in-situ exploration missions.

4. Analysis and Applications

4.1 Discussion on Optical Reflectance of Rocks

After impact events (such as meteorite impacts and volcanic eruptions), a large number of glass spheres (meteorite glass and volcanic glass) and rock fragments are generated, which have high specular reflection coefficients (Wang et al., 2024a). From Kaguya data, the albedo A of rock is larger than the neighboring lunar regolith. To further explain the differences in intensity I between rocks and lunar regolith at different illumination angles, Fig. 13 shows the relationship between the image intensity I of rocks and lunar regolith as a function of solar incident angle with Equation 1.

According to Kaguya data, the average albedo of rocky areas is set to be 0.048 and the average albedo of lunar regolith is set to be 0.034. Here, it is assumed that $\theta_t = 0$. The variation of I for rocks and lunar regolith with different solar incident angle is calculated.

In Fig. 13, at small illumination angles, there is $\cos(\theta_i) \approx 1$, $G(\theta_i, \theta_e) \approx 1$, and $I \approx A$. The intensity I of rocks is greater than that of lunar regolith by 0.013. As the solar incident angle increases, the image intensities I of lunar regolith and rocks decrease. At large incident angles between 70° and 90°, the difference in intensity I between rocks and lunar regolith is less than 0.002. Consequently, at large incident angles, the distribution of rocks is difficult to identify.

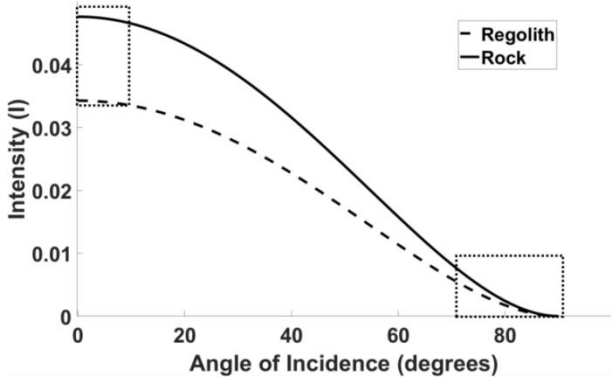

Fig. 13. A curve graph showing the variation of image intensity with incident angle. The curves illustrate the relationship between the image intensity of lunar regolith and rock as a function of solar incident angle.

4.2 Strong Radar Backscattering from Rocks

Different from optical cameras, SAR is sensitive to rock and undulated topography. In order to understand SAR images, SAR images with or without rocks are simulated, and compared with measured data for validation.

Fig. 14a shows the SAR image of the fresh crater in Fig. 4, where distinct rock ejecta blanket can be observed. The red mask in Fig. 14b is the ejecta blanket extracted from the SAR image, overlaid on the LROC NAC optical image at a small solar illumination angle. It can be seen that the rock ejecta blanket in the SAR image is consistent with that in the optical image. Fig. 14c is the slope angle map of this area. Figs. 14d-f are enlarged images of the red box, which present the distribution of surface rocks.

In the simulation, the 3D morphology is constructed by DTM. The lunar topography is divided into small triangular meshes. The vertices of these triangles are defined by neighboring points from the DTM data. The raw data is simulated by KA-SPM dual-

scale model, and the imaging is performed by Range-Doppler algorithm (Liu and Jin, 2023). The components S_{pq}^{n} of the scattering matrix for mesh n depend on the area and reflectivity of that mesh. Therefore, S_{pq}^{n} can be expressed as (Ulaby et al., 2014):

$$S_{pq}^{n} = \gamma_{pq}^{n}\sqrt{\frac{A_n}{4\pi}} \tag{10}$$

where γ_{pq}^{n} is the reflectivity from the mesh n. A_n is the area of the mesh n. The subscript q is the transmitted polarization and p is the received polarization. γ_{pq} is simulated by KA-SPM two-scale model (Liu and Jin, 2022).

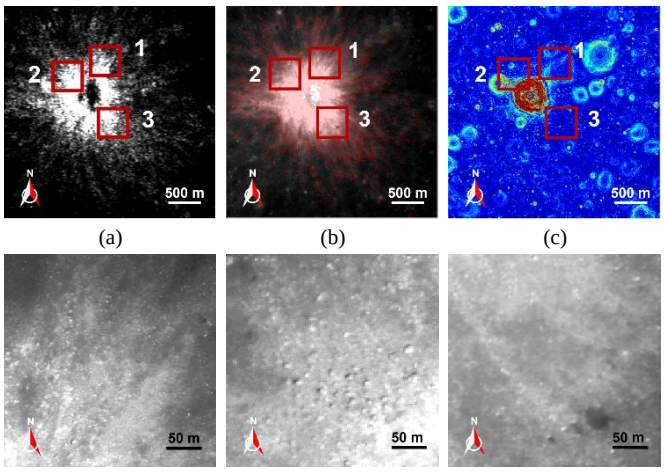

Fig. 14. Qualitative analysis of rock ejecta blanket in SAR and optical images. (a-c) The rock ejecta blanket of fresh crater in the SAR, optical image, and slope angle map, respectively. The red mask in Fig. b indicates the rock ejecta blanket from SAR, which is consistent with the optical image in Fig. a. (d-f) A high-resolution optical image displays three different rock distributions. There are clear boundaries of the rocks in red box 1. There is a larger and denser rock distribution in red box 2. And in red box 3, there is a sparse rock distribution.

In SAR simulation, the raw signals can be written as (Shimada, 2019):

$$h_{pq}(t,T) = \sum S_{pq}^{n} s^{n}(t,T) \tag{11}$$

where a chirp modulation pulse is transmitted. There is

$$s^{n}(t,T) = \prod\left[\frac{t-2R^{n}/c}{\tau/2}\right]\prod\left[\frac{vT-x^{n}}{L_s/2}\right]\exp\left\{-i4\pi\frac{R^{n}}{\lambda}+i\pi K_r\left(t-\frac{2R^{n}}{c}\right)^{2}\right\}n \tag{12}$$

$$\prod(t) = \begin{cases} 1 & |t| \le 1 \\ 0 & |t| > 1 \end{cases} \tag{13}$$

where τ represents the pulse width, t is the time, v is the speed of the satellite, T is the azimuth time, x^{n} is the azimuth coordinate of the mesh n, R^{n} is the distance between the antenna and the mesh n, c is the speed of light in vacuum, λ is the wavelength, K_r is the chirp rate, $L_s = \lambda R / L_A$ is the real antenna azimuth footprint (Liu and Jin, 2023). The Range-Doppler algorithm is used to generate SAR images.

Figs. 15a and b show the simulated SAR image with and without rocks. The resolution of the simulated SAR images is 15 m/pixel. The DTM slope map in Fig. 14c cannot capture rock information. Therefore, a rough surface with $L = 15m$ and $\delta = 2m$ is overlaid in the rock ejecta blanket of the DTM to model the rocky surface (Liu and Jin, 2023). The rocky surface alters the radar incidence angle. The backscattering from patches with small incidence angles is significantly enhanced, resulting in a stronger overall echo from the rocky area. Additionally, multiple scattering from large granular structures can also enhance backscattering, though this mechanism was not included in the current simulation.

Additionally, multiple scattering from large granular structures can also enhance backscattering, though this mechanism was not included in the current simulation.

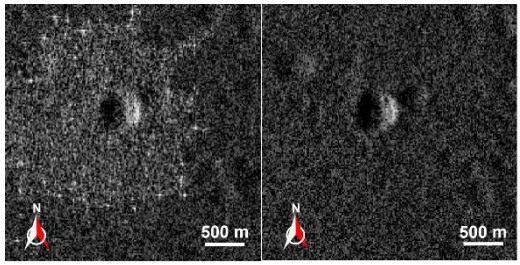

(a) (b)

Fig. 15. Simulation Results. (a) SAR image with rocks, showing distinct rock ejecta blanket. (b) SAR image without rocks, lacking rock ejecta blanket.

4.3 *Identification of Rocky Craters Using LunarS2O*

This study investigates the relationship between rock distribution and radar backscattering intensity in lunar craters. In SAR imagery, areas of high backscattering are influenced by both topographic orientation and surface roughness. Slopes facing the radar exhibit higher backscattering intensity, whereas those facing away from the radar show weaker signals due to shadowing effects (Fa and Cai, 2013; Liu and Jin, 2023).

Fig. 16a presents an measured LROC NAC optical image (25 cm/pixel) near the Apollo 17 landing site at (20.09°N, 30.75°E), showing crater walls with randomly distributed coarse boulder fields (Robinson et al., 2010). Fig. 16b shows the corresponding SAR image of this region at 14.8 m/pixel resolution, with an arrow indicating the Mini-RF illumination direction (Nozette et al., 2010). Fig. 16c displays manually annotated 8 boulder distributions on the crater walls. Comparative analysis between low-latitude high-resolution optical images and SAR data reveals a strong spatial consistency between boulder fields in Fig. 16a and high-backscattering regions in Fig. 16b. On crater walls with similar slopes facing the radar in red box, surfaces with coarse boulder fields show significantly enhanced backscattering intensity. In radar-shadowed regions, although the overall backscattering is relatively weak, areas with boulder fields still exhibit higher intensity compared to adjacent areas. These observations confirm a positive correlation between boulder presence and backscattering intensity. The results indicate that variations in high-backscattering patterns in SAR images correlate not only with crater wall slope but also positively with boulder field distribution.

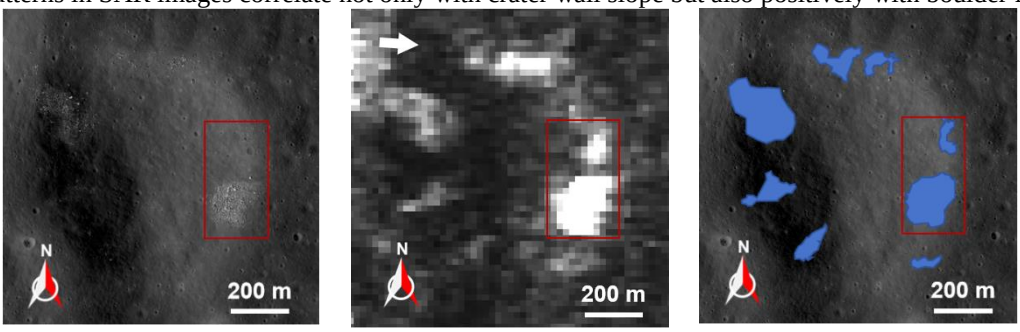

(a) (b) (c)

Fig. 16. Correlation analysis between crater boulder distribution and SAR backscattering characteristics. (a) Optical image near the Apollo 17 landing site (25 m/pixel) showing coarse boulder fields on crater walls. (b) Corresponding SAR image (14.8 m/pixel resolution) with white arrow indicating Mini-RF illumination direction. (c) Manually annotated boulder distributions on crater walls. Comparative analysis confirms spatial consistency between boulder fields and high SAR backscattering regions, with a positive correlation between boulder presence and backscattering intensity.

To validate the reliability of boulder-bearing craters in the LunarS2O optical imagery, a comparative analysis was conducted with very high-resolution LROC NAC images (25 cm/pixel). Fig. 17 presents a comparison for a region near the Apollo 17 landing site, displaying from left to right: the SAR image, the LunarS2O optical image, the LROC NAC optical image, and a zoomed-in LROC NAC view. Craters identified in both the LunarS2O and LROC NAC images are manually annotated with red circles. The zoomed-in LROC NAC view in red box confirms that the red-circled crater contains distinct boulder fields at its bottom in white polygon. Conversely, crater present in the NAC image but absent from the LunarS2O image is marked with blue circle. The blue-circled crater generally exhibits smoother textures in the LROC NAC image, with no obvious rock distributions.

The comparative results demonstrate that the craters generated by this method correspond to those containing rough boulder fields. Consequently, the LunarS2O imagery effectively reveals surface rock information of the craters.

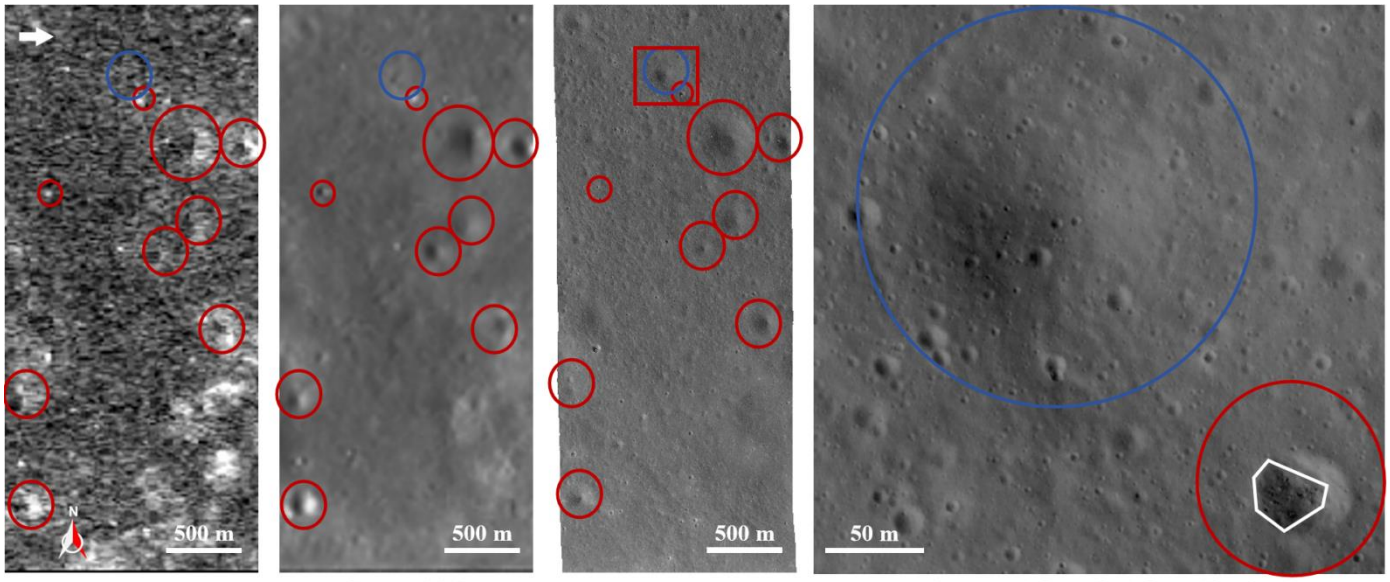

Fig. 17. Validation of crater boulder distribution in generated optical imagery. From left to right: SAR image, LunarS2O optical image, LROC NAC optical image (25 cm/pixel) and its zoomed-in view. Red circles mark craters with boulder fields identified in both LunarS2O and NAC images. Blue circle mark craters without boulder fields present only in NAC images. Results demonstrate the method's effectiveness in identifying craters with rough boulder fields and accurately revealing surface rock information.

Based on these findings, a systematic comparative analysis was conducted between the LunarS2O imagery and ShadowCam observations in the lunar south polar PSRs. Fig. 18 shows PSRs larger than 1 km² in Sverdrup crater. The blue line is the PSR boundary (Mazarico et al., 2011). The red box located at (88.33°S, 218.58°E). Craters identified in both the LunarS2O and ShadowCam images (marked with red circles) indicate the presence of coarse boulder fields within these craters. The absence of certain ShadowCam-observed craters (green circles) in the LunarS2O imagery suggests a lack of significant coarse boulder distributions. Additionally, some features present only in the LunarS2O images but absent in ShadowCam data may be attributed to potential water ice deposits or sub-pixel-scale rock. Within the area, 48 craters exceeding 0.15 km in diameter were identified. Among these, 40 well-preserved craters interpret as boulder fields while 8 exhibit degradation.

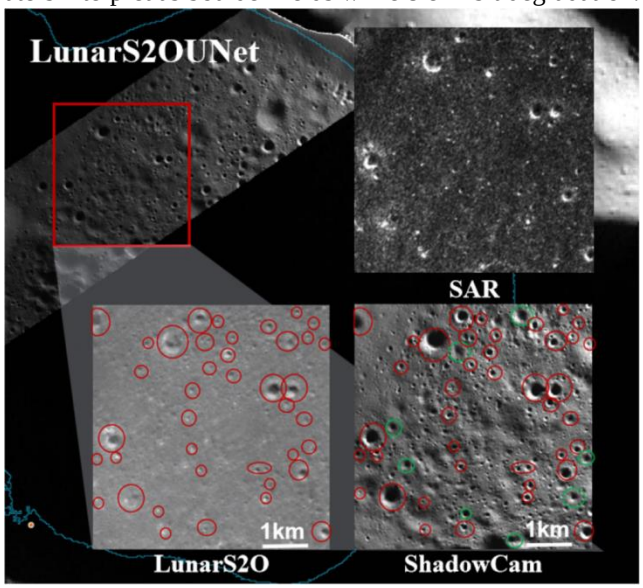

Fig. 18. Comparison of LunarS2O and ShadowCam images in PSR of lunar south pole.

It should be noted that the correlation between high SAR backscattering and boulder distribution is not exclusive. Other factors can produce similar scattering signatures. For instance, large-scale slopes of massive craters facing the radar may generate strong backscattering through geometric reflection. Within ejecta blankets of fresh craters, densely distributed centimeter-to-meter-scale rocks could collectively enhance backscattering even when individual boulders are visually indistinguishable. Furthermore, the

inherent dielectric properties of different geological contexts (e.g., basaltic flows versus fractured highland materials) influence regional backscattering intensity.

Despite these complexities, the relationship between SAR backscattering and optical characteristics revealed through the LunarS2O offers a new technical perspective for detecting surface roughness and boulder distributions in challenging environments like PSRs. This approach complements single-data-source limitations and provides valuable supplementary information for future lunar geological studies and precise landing site selection.

4.4 SAR-Optical Heterogeneous Registration

Lunar remote sensing encompasses diverse imaging modes and multi-source data, making precise cross-source data co-registration essential for deep space exploration and lunar research (Wagner et al., 2015). SAR images, in particular, present challenges in processing and application due to geometric distortions inherent to the imaging principle, often resulting in low efficiency and limited applicability. Traditional homogeneous registration methods, which are ill-suited for S2O data alignment, frequently yield suboptimal alignment and seldom achieve high-precision, pixel-level co-registration. Consequently, improving the registration accuracy between SAR and optical imagery has become a key research focus (Dellinger et al., 2015).

This study presents a homologous registration approach based on LunarS2O images. By precisely aligning the LunarS2O images with existing high-resolution lunar optical data, pixel-level co-registration between the original SAR and optical images is achieved. The method first extracts key points using the Scale-Invariant Feature Transform (SIFT) algorithm (Lowe, 1999; Lowe, 2004), followed by initial matching with the Random Sample Consensus (RANSAC) (Fischler and Bolles, 1981). An iterative refinement process involving two rounds of affine transformation is then applied to align the LunarS2O and reference optical images. The same transformation is subsequently applied to the original SAR data, enabling its precise registration to the target optical image. This systematic procedure enables precise heterogeneous data registration through generated optical imagery as an intermediate bridge, effectively mitigating registration challenges.

To evaluate the practical application value of LunarS2O imagery in heterogeneous remote sensing data registration, registration experiments were conducted. Fig. 19a shows the registered SAR image, where the original SAR with 14.8 m/pixel resolution has undergone a rotation of 42.67° to achieve alignment. Fig. 19b displays the optical reference image of the target area, serving as the registration benchmark. Through two-stage SIFT feature matching and affine transformation optimization, precise spatial transformation parameters were ultimately obtained. The feature matching process extracted 21 high-precision inliers retained after RANSAC optimization.

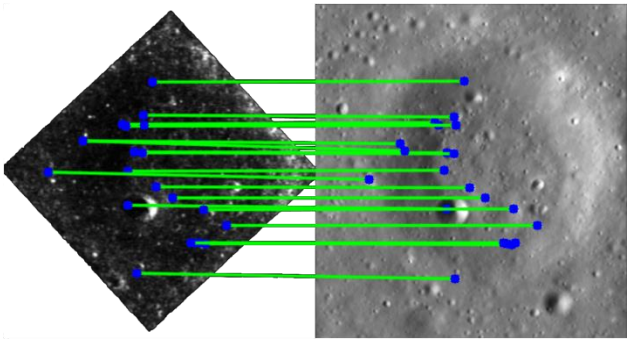

(a) (b)

Fig. 19. Validation of heterogeneous data registration based on LunarS2O imagery. (a) Registered SAR image result after applying the transformation. (b) Target optical reference image. Feature matching achieved 21 inliers, realizing pixel-level registration accuracy.

Experimental results indicate that the registration method based on LunarS2O imagery overcomes modal differences between SAR and optical images, providing a possible technical approach for spatial alignment of heterogeneous remote sensing data. It should be noted that the application condition of this registration method is limited. When the LunarS2O and reference images share identical illumination geometry, the performance is high, while it degrades under different illumination conditions.

V. Conclusion

The PSRs on the lunar poles lack direct solar illumination, and scattered light angles typically exceed 70°, making it challenging for optical instruments such as ShadowCam to observe interior SSR and distribution of rocks. To address this limitation, this study presents LunarS2OUNet, a solution for converting S2O images with matching incidence geometry in PSRs.

Addressing the scarcity of paired SAR and optical images of the Moon, optical imagery corresponding to the incidence direction and angle of SAR data were simulated using a linear combination of the Lambert and the Lommel–Seeliger model. The LOSAD-14k containing 14,000 multi-scale image pairs was constructed. The trained LunarS2OUNet effectively performs S2O image translation with LGAM and LOSAD-14k.

Compared with ShadowCam images, the generated low-incidence-angle optical images reveal the topographic structure and rock distribution within PSRs, particularly enabling visualization of SSR internal morphology otherwise unobtainable through conventional optical imaging. In application, the generated imagery also successfully distinguishes between craters with and without boulders, providing a methodology for identifying anomalous areas in PSRs. Furthermore, the synthetic optical images enable pixel-level co-registration of SAR and optical images, offering a new approach for heterogeneous remote sensing data alignment. Simulation experiments confirm that the detectability of rock remains consistent across different incidence angles in both SAR and the generated optical images, with the results reflecting the distribution of rocks.

It should be noted that the quality of the generated optical imagery depends on the spatial resolution of the input SAR data. With future acquisitions of higher-resolution SAR imagery in Chang'e-7, the precision and detail of the generated images are expected to see significant improvement.

ACKNOWLEDGMENT

The Mini-RF, ShadowCam, and LROC data products utilized in this study are archived and distributed through the Planetary Data System (PDS) Geosciences Node at http://pds-geosciences.wustl.edu and the Orbital Data Explorer (ODE) at https://ode.rsl.wustl.edu/moon/mapsearch. Kaguya (SELENE) data were obtained from the JAXA Data Archive and Transmission System at https://darts.isas.jaxa.jp/app/pdap/selene/index.html.en. This work was supported in part by the National Natural Science Foundation of China under Grant 62495032 and Grant 62201154, and in part the Chenguang Program of Shanghai Education Development Foundation and Shanghai Municipal Education Commission.

REFERENCES

Bai, X., Pu, X., Xu, F., 2024. Conditional Diffusion for SAR to Optical Image Translation. IEEE Geoscience and Remote Sensing Letters. 21**,** 1-5.

Bickel, V. T., Moseley, B., Lopez-Francos, I., Shirley, M., 2021. Peering into lunar permanently shadowed regions with deep learning. Nature Communications. 12**,** 5607.

Bray, V. J., Collins, G. S., Morgan, J. V., Schenk, P. M., 2008. The effect of target properties on crater morphology: Comparison of central peak craters on the Moon and Ganymede. Meteoritics & Planetary Science. 43**,** 1979-1992.

Brown, H. M., Boyd, A. K., Sonke, A., Huft, A., Robinson, M. S., Cisneros, E., 2022. Lunar Reconnaissance Orbiter Camera Permanently Shadowed Region Images: Updates to PSR Atlas and PSR Mosaics. Lunar Polar Volatiles Conference, Vol. 2703, Boulder, Colorado, pp. 5033.

Bussey, D. B. J., et al., 2010. Illumination conditions of the south pole of the Moon derived using Kaguya topography. Icarus. 208**,** 558-564.

Cahill, J. T. S., et al., 2014. The Miniature Radio Frequency instrument's (Mini-RF) global observations of Earth's Moon. Icarus. 243**,** 173-190.

Campbell, D. B., Campbell, B. A., Carter, L. M., Margot, J.-L., Stacy, N. J. S., 2006. No evidence for thick deposits of ice at the lunar south pole. Nature. 443**,** 835-837.

Carrer, L., Pozzobon, R., Sauro, F., Castelletti, D., Patterson, G. W., Bruzzone, L., 2024. Radar evidence of an accessible cave conduit on the Moon below the Mare Tranquillitatis pit. Nature Astronomy. 8**,** 1119-1126.

Carruba, V., Coradini, A., 1999. Lunar Cold Traps: Effects of Double Shielding. Icarus. 142**,** 402-413.

Dellinger, F., Delon, J., Gousseau, Y., Michel, J., Tupin, F., 2015. SAR-SIFT: A SIFT-Like Algorithm for SAR Images. IEEE Transactions on Geoscience and Remote Sensing. 53**,** 453-466.

Di, K., Sun, S., Yue, Z., Liu, B., 2016. Lunar regolith thickness determination from 3D morphology of small fresh craters. Icarus. 267**,** 12-23.

Eskicioglu, A. M., Fisher, P. S., 1995. Image quality measures and their performance. IEEE Trans. Commun. 43**,** 2959-2965.

Fa, W., Cai, Y., 2013. Circular polarization ratio characteristics of impact craters from Mini-RF observations and implications for ice detection at the polar regions of the Moon. Journal of Geophysical Research: Planets. 118**,** 1582-1608.

Fa, W., Eke, V. R., 2018. Unravelling the Mystery of Lunar Anomalous Craters Using Radar and Infrared Observations. Journal of Geophysical Research: Planets. 123**,** 2119-2137.

Fassett, C. I., et al., 2024. The LCROSS Impact Crater as Seen by ShadowCam and Mini-RF: Size, Context, and Excavation of Copernican Volatiles. Geophysical Research Letters. 51**,** e2024GL110355.

Fischler, M. A., Bolles, R. C., 1981. Random sample consensus: a paradigm for model fitting with applications to image analysis and automated cartography. Commun. ACM. 24**,** 381–395.

Fu, S., Xu, F., Jin, Y.-Q., 2021. Reciprocal translation between SAR and optical remote sensing images with cascaded-residual adversarial networks. Science China Information Sciences. 64**,** 122301.

Girshick, R., 2015. Fast R-CNN. 2015 IEEE International Conference on Computer Vision (ICCV), pp. 1440-1448.

Goodfellow, I. J., et al., 2014. Generative adversarial nets. Proceedings of the 28th International Conference on Neural Information Processing Systems - Volume 2, Vol. 2. MIT Press, Montreal, Canada, pp. 2672–2680.

He, K., Zhang, X., Ren, S., Sun, J., 2015. Deep Residual Learning for Image Recognition. 2016 IEEE Conference on Computer Vision and Pattern Recognition (CVPR). 770-778.
Herrick, R. R., Forsberg-Taylor, N. K., 2003. The shape and appearance of craters formed by oblique impact on the Moon and Venus. Meteoritics & Planetary Science. 38**,** 1551-1578.
Ho, J., Jain, A., Abbeel, P., 2020. Denoising Diffusion Probabilistic Models.
Hofgartner, J. D., Hand, K. P., 2023. A continuum of icy satellites' radar properties explained by the coherent backscatter effect. Nature Astronomy. 7**,** 534-540.
Hu, J., Shen, L., Sun, G., Albanie, S., 2017. Squeeze-and-Excitation Networks. IEEE Transactions on Pattern Analysis and Machine Intelligence. PP.
Isola, P., Zhu, J. Y., Zhou, T., Efros, A. A., 2017. Image-to-Image Translation with Conditional Adversarial Networks. 2017 IEEE Conference on Computer Vision and Pattern Recognition (CVPR), pp. 5967-5976.
Johnson, J., Alahi, A., Fei-Fei, L., 2016. Perceptual Losses for Real-Time Style Transfer and Super-Resolution. In: B. Leibe, J. Matas, N. Sebe, M. Welling, (Eds.), Computer Vision – ECCV 2016. Springer International Publishing, Cham, pp. 694-711.
Kato, M., Sasaki, S., Takizawa, Y., the Kaguya project, t., 2010. The Kaguya Mission Overview. Space Science Reviews. 154**,** 3-19.
Kaydash, V., Shkuratov, Y., Videen, G., 2014. Dark halos and rays of young lunar craters: A new insight into interpretation. Icarus. 231**,** 22-33.
Li, H., Gu, C., Wu, D., Cheng, G., Guo, L., Liu, H., 2022. Multiscale Generative Adversarial Network Based on Wavelet Feature Learning for SAR-to-Optical Image Translation. IEEE Transactions on Geoscience and Remote Sensing. 60**,** 1-15.
Liu, N., Jin, Y. Q., 2022. Simulation of Pol-SAR Imaging and Data Analysis of Mini-RF Observation From the Lunar Surface. IEEE Transactions on Geoscience and Remote Sensing. 60**,** 1-11.
Liu, N., Jin, Y. Q., 2023. Pol-SAR Image Simulation of the Lunar Surface With Data Analysis of Chandrayaan-2 and Mini-RF. IEEE Journal of Selected Topics in Applied Earth Observations and Remote Sensing. 16**,** 10301-10310.
Lohse, V., Heipke, C., Kirk, R. L., 2006. Derivation of planetary topography using multi-image shape-from-shading. Planetary and Space Science. 54**,** 661-674.
Lowe, D. G., 1999. Object recognition from local scale-invariant features. Proceedings of the seventh IEEE international conference on computer vision, Vol. 2. Ieee, pp. 1150-1157.
Lowe, D. G., 2004. Distinctive Image Features from Scale-Invariant Keypoints. International Journal of Computer Vision. 60**,** 91-110.
Mahendran, A., Vedaldi, A., 2014. Understanding deep image representations by inverting them. 2015 IEEE Conference on Computer Vision and Pattern Recognition (CVPR). 5188-5196.
Mazarico, E., Neumann, G. A., Smith, D. E., Zuber, M. T., Torrence, M. H., 2011. Illumination conditions of the lunar polar regions using LOLA topography. Icarus. 211**,** 1066-1081.
McEwen, A. S., 1991. Photometric functions for photoclinometry and other applications. Icarus. 92**,** 298-311.
Merkle, N., Auer, S., Müller, R., Reinartz, P., 2018. Exploring the Potential of Conditional Adversarial Networks for Optical and SAR Image Matching. IEEE Journal of Selected Topics in Applied Earth Observations and Remote Sensing. 11**,** 1811-1820.
Nozette, S., et al., 2010. The Lunar Reconnaissance Orbiter Miniature Radio Frequency (Mini-RF) Technology Demonstration. Space Science Reviews. 150**,** 285-302.
Paige, D. A., et al., 2010. Diviner Lunar Radiometer Observations of Cold Traps in the Moon's South Polar Region. Science. 330**,** 479-482.
Qin, J., Wang, K., Zou, B., Zhang, L., Weijer, J. v. d., 2024. Conditional Diffusion Model With Spatial-Frequency Refinement for SAR-to-Optical Image Translation. IEEE Transactions on Geoscience and Remote Sensing. 62**,** 1-14.
Robinson, M. S., et al., 2023. ShadowCam Instrument and Investigation Overview. Journal of Astronomy and Space Sciences. 40**,** 149-171.
Robinson, M. S., et al., 2010. Lunar Reconnaissance Orbiter Camera (LROC) Instrument Overview. Space Science Reviews. 150**,** 81-124.
Ronneberger, O., Fischer, P., Brox, T., 2015. U-Net: Convolutional Networks for Biomedical Image Segmentation. In: N. Navab, J. Hornegger, W. M. Wells, A. F. Frangi, (Eds.), Medical Image Computing and Computer-Assisted Intervention – MICCAI 2015. Springer International Publishing, Cham, pp. 234-241.
Rudin, L. I., Osher, S., Fatemi, E., 1992. Nonlinear total variation based noise removal algorithms. Physica D: Nonlinear Phenomena. 60**,** 259-268.
Shimada, M., 2019. Imaging from Spaceborne and Airborne SARs, Calibration, and Applications. Journal of The Remote Sensing Society of Japan. 39**,** 323-323.
Smith, D. E., et al., 2017. Summary of the results from the lunar orbiter laser altimeter after seven years in lunar orbit. Icarus. 283**,** 70-91.
Speyerer, E. J., Robinson, M. S., Denevi, B. W., Team, L. S., 2011. Lunar Reconnaissance Orbiter Camera Global Morphological Map of the Moon. 42nd Annual Lunar and Planetary Science Conference, The Woodlands, Texas, pp. 2387.
Tang, P., et al., 2025. Simulation of Subsurface Physical Temperatures in Lunar Craters Using Solar Irradiance, Infrared and Microwave Data. IEEE Transactions on Geoscience and Remote Sensing. 63**,** 1-16.

Tye, A. R., et al., 2015. The age of lunar south circumpolar craters Haworth, Shoemaker, Faustini, and Shackleton: Implications for regional geology, surface processes, and volatile sequestration. Icarus. 255**,** 70-77.

Ulaby, F., et al., 2014. Microwave Radar and Radiometric Remote Sensing.

Ulyanov, D., Vedaldi, A., Lempitsky, V., 2016. Instance Normalization: The Missing Ingredient for Fast Stylization.

Wagner, R. V., Speyerer, E. J., Robinson, M. S., Team, L., 2015. New Mosaicked Data Products from the LROC Team. 46th Annual Lunar and Planetary Science Conference, The Woodlands, Texas, pp. 1473.

Wang, B.-W., et al., 2024a. Returned samples indicate volcanism on the Moon 120 million years ago. Science. 385**,** 1077-1080.

Wang, C., et al., 2024b. Scientific objectives and payload configuration of the Chang'E-7 mission. National Science Review. 11**,** nwad329.

Wang, T. C., Liu, M. Y., Zhu, J. Y., Tao, A., Kautz, J., Catanzaro, B., 2018. High-Resolution Image Synthesis and Semantic Manipulation with Conditional GANs. 2018 IEEE/CVF Conference on Computer Vision and Pattern Recognition, pp. 8798-8807.

Wang, Z., Bovik, A. C., Sheikh, H. R., Simoncelli, E. P., 2004. Image quality assessment: from error visibility to structural similarity. IEEE Trans Image Process. 13**,** 600-12.

Wu, B., Liu, W. C., Grumpe, A., Wöhler, C., 2018. Construction of pixel-level resolution DEMs from monocular images by shape and albedo from shading constrained with low-resolution DEM. ISPRS Journal of Photogrammetry and Remote Sensing. 140**,** 3-19.

Xia, T., Ren, X., Liu, Y., Liu, N., Xu, F., Jin, Y.-Q., 2024. Detection of Surface Rocks and Small Craters in Permanently Shadowed Regions of the Lunar South Pole Based on YOLOv7 and Markov Random Field Algorithms in SAR Images. Remote Sensing, Vol. 16.

Yin, Z., Liu, N., Jin, Y.-Q., 2024. Simulation of the temperatures in the permanently shadowed region of the Moon's south pole and data validation. Icarus. 411**,** 115917.

Zhang, R., Isola, P., Efros, A. A., Shechtman, E., Wang, O., 2018. The Unreasonable Effectiveness of Deep Features as a Perceptual Metric. 2018 IEEE/CVF Conference on Computer Vision and Pattern Recognition. 586-595.

Zhao, H., Shi, J., Qi, X., Wang, X., Jia, J., 2017. Pyramid Scene Parsing Network. 2017 IEEE Conference on Computer Vision and Pattern Recognition (CVPR). IEEE Computer Society, pp. 6230-6239.

Zhong, Z., Yang, Z., Liu, B., Yan, J., Wang, J., Zhang, L., 2025. Illumination and regolith temperature for China's candidate lunar landing sites with multiple scattering considerations. Icarus. 430**,** 116488.

Zhou, W., Bovik, A. C., Sheikh, H. R., Simoncelli, E. P., 2004. Image quality assessment: from error visibility to structural similarity. IEEE Transactions on Image Processing. 13**,** 600-612.

Zhu, J. Y., Park, T., Isola, P., Efros, A. A., 2017. Unpaired Image-to-Image Translation Using Cycle-Consistent Adversarial Networks. 2017 IEEE International Conference on Computer Vision (ICCV), pp. 2242-2251.

Declaration of interests

The authors declare that they have no known competing financial interests or personal relationships that could have appeared to influence the work reported in this paper.